# Imaging *ex vivo* healthy and pathological human brain tissue with ultra-high-resolution optical coherence tomography

**Kostadinka Bizheva**
**Angelika Unterhuber**
**Boris Hermann**
**Boris Považay**
**Harald Sattmann**
**A. F. Fercher**
Medical University of Vienna
and Christian Doppler Laboratory
Center for Biomedical Engineering and Physics
Vienna A-1090, Austria

**Wolfgang Drexler**
Medical University of Vienna
and Christian Doppler Laboratory
Center for Biomedical Engineering and Physics
Waehringer Strasse 13
Vienna A-1090, Austria
E-mail: Wolfgang.Drexler@meduniwler@ac.at

**Matthias Preusser**
**Herbert Budka**
Medical University of Vienna
and Vienna General Hospital
Institute of Neurology
Vienna A-1090, Austria

**Andreas Stingl**
**Tuan Le**
FEMTOLASERS GmbH
Fernkorngasse 10
Vienna A-1100, Austria

**Abstract.** The ability of ultra-high-resolution optical coherence tomography (UHR OCT) to discriminate between healthy and pathological human brain tissue is examined by imaging *ex vivo* tissue morphology of various brain biopsies. Micrometer-scale OCT resolution (0.9×2 $\mu$m, axial×lateral) is achieved in biological tissue by interfacing a state-of-the-art Ti:$Al_2O_3$ laser ($\lambda_c$=800 nm, $\Delta\lambda$=260 nm, and $P_{out}$=120 mW exfiber) to a free-space OCT system utilizing dynamic focusing. UHR OCT images are acquired from both healthy brain tissue and various types of brain tumors including fibrous, athypical, and transitional meningioma and ganglioglioma. A comparison of the tomograms with standard hematoxylin and eosin (H&E) stained histological sections of the imaged biopsies demonstrates the ability of UHR OCT to visualize and identify morphological features such as microcalcifications (>20 $\mu$m), enlarged nuclei of tumor cells (~8 to 15 $\mu$m), small cysts, and blood vessels, which are characteristic of neuropathologies and normally absent in healthy brain tissue.
 [DOI: 10.1117/1.1851513]

Keywords: optical coherence tomography; biomedical optics; medical imaging; brain imaging.

Paper NEU-10 received Feb. 20, 2004; revised manuscript received Jul. 1, 2004; accepted for publication Aug. 8, 2004; published online Jan. 31, 2005.

## 1 Introduction

In neurosurgery, the goal of any intracranial intervention is to provide accurate localization, diagnosis, and an appropriate treatment of intracranial abnormalities, while causing minimal damage to the intact brain. During open-skull surgery, the boundaries of some lesions, in particular some gliomas, as well as the presence and location of small brain tumors may be difficult to determine by means of visual inspection or microscopic imaging of the tissue surface. In the past a number of nonoptical imaging methods[1–9] such as magnetic resonance imaging (MRI), ultrasound, and computed tomography (CT) have been used to identify the margins of large brain tumors and to locate clusters of tumor cells positioned farther away. Although these imaging modalities enable noninvasive tumor diagnostics, they suffer from two major disadvantages: poor spatial resolution (hundreds of micrometers to a few millimeters), insufficient for resolving small brain tumors, and misalignment between the imaged and actual positions of the tumor due to tissue movement during surgery.[10] Recently, there has been a constant demand for the development of noninvasive or minimally invasive optical imaging techniques that can be applied in neurosurgery as guiding tools and as an alternative to standard excisional biopsy. Imaging methods such as diffuse optical tomography, reflectance imaging, near-IR and Raman spectroscopy, fluorescence, and confocal microscopy[11–15] have enabled visualization of single tumor cells as well as better delineation of brain tumor borders. Despite all these advantages, each of these imaging modalities possesses some inherent limitation related to image resolution, acquisition time, specificity, and accuracy of the acquired image/information, etc., which motivates the constant search for novel more precise and less invasive imaging modalities.

Optical coherence tomography (OCT) is a noncontact optical imaging method that combines micrometer-scale resolution with millimeter image penetration depth[16–18] and as such may have a potential as a guiding and/or diagnostic tool in neurosurgery. Although OCT has been successfully applied to many biomedical problems in ophthalmology, dermatology, gastroenterology, etc.[19] since its invention about a decade ago, so far only a few attempts[20–23] have been made to image brain tissue morphology and function with standard-resolution

1083-3668/2005/$22.00 © 2005 SPIE

OCT. A common disadvantage in all these studies was the fact that the spatial resolution (axial resolution ~10 to 15 $\mu$m) was insufficient to enable visualization of fine morphological details such as microcalcifications, anaplasia, etc. that are characteristic of various types of brain tumors. Recent advances[24–30] in laser technology have led to the development of ultra-high-resolution (UHR) OCT (axial resolution $<2$ $\mu$m) and current research in ophthalmology has clearly demonstrated the feasibility of UHR OCT to image intraretinal morphology as well as to view small structural features in intraocular pathologies.[31–33] A very recent study[34] has also demonstrated the ability of OCT with axial resolution below 2 $\mu$m to image animal brain tissue morphology on the scale from singe cells to whole brains as well as to visualize clearly both glandular and layered tissue structures the size of a few tens of micrometers.

The objective of this research project was to investigate the ability of UHR OCT to discriminate between healthy and pathological human brain tissue by visualization of fine morphological features characteristic for neuropathologies and normally absent in healthy brain tissue. In addition, this study aimed to establish a correlation between structural details present in both the OCT tomograms and in the corresponding histological cross sections.

## 2 Methods

Submicrometer axial OCT resolution in biological tissue was achieved by interfacing a state-of-the-art, prismless Ti:$Al_2O_3$ laser[35] (center wavelength $\lambda_c = 800$ nm, spectral bandwidth $\Delta\lambda = 260$ nm, and output power $P_{out} = 120$ mW, exfiber) to a free-space OCT system previously described in Ref. 28. All-optical and fiber optic components were selected to support propagation of broadband light through the system with minimal spectral and power losses in the range of 600 to 1000 nm, as well as to compensate for any polarization and dispersion mismatch between the sample and reference arm of the interferometer. Dynamic focusing was implemented to prevent loss of image transverse resolution deeper in the tissue sample resulting from beam defocusing. The OCT system was evaluated to provide $1.3\times3$ $\mu$m (axial$\times$lateral) resolution in air, ideally corresponding to $0.9\times2$ $\mu$m in biological tissue, and sensitivity of 112 dB for 5 mW at the sample surface. Full fringe detection was realized by use of a high-speed (10 Ms/s), 16-bit analog-to-digital (A/D) converter (Gage Appl. Tech.) to digitize the fringe data, thus enabling extraction of functional and spectroscopic information in addition to the high-resolution morphological imaging.

For the purpose of this paper, fixed tissue samples were obtained from healthy brain tissue as well as from various brain tumors including transitional, fibrous, and atypical meningioma and ganglioglioma. It is well known that formalin fixation alters the optical properties of biological tissue, however, the choice of imaging fixed brain tissue in this preliminary study was governed by two major reasons: first, fresh human healthy brain tissue is not readily available, and second, postmortem brain tissue quickly looses optical quality due to cell death even when preserved in saline or buffer solution for a time period longer than few hours. All tissue samples used in this study were obtained through the following protocol: healthy human brain tissue sections were prepared from whole brains that were fixed in formalin within 3 to 6 h postmortem during autopsy (standard procedure for obtaining tissue samples for anatomy/neuropathology studies). All tumor samples imaged with OCT were obtained by cutting a small section from the brain tissue biopsies extracted during neurosurgery and originally intended for neuropathological analysis. To be consistent in comparing the optical properties and morphological appearance in the OCT tomograms of healthy and pathological brain tissue, the neuropathological samples were also fixed in formalin immediately after excision.

The tissue samples were placed in a custom-designed chamber with an optical window (~150-$\mu$m-thick glass cover slip), through which the tissue was imaged. During the imaging procedure, care was taken to properly compensate the dispersion mismatch introduced by the glass cover slip and the excess fixation solution between the glass and the tissue surface to preserve the high OCT axial resolution. The imaged regions were carefully marked on digital photographs of the tissue samples and subsequently hematoxylin and eosin (H&E) stained histological sections were obtained from them. Typically, 10 to 30 UHR OCT tomograms were acquired from each tissue sample, and for each type of brain tumor, a number of biopsies obtained from different patients were examined (fibrous meningioma, 3; atypical meningioma, 3; ganglioglioma, 2).

## 3 Results

Multiple UHR OCT tomograms were acquired from formalin-fixed healthy human brain tissue to be used as a baseline reference for morphological comparison with images acquired from various brain tumor biopsies. A representative OCT image from the normal brain tissue is shown in Fig. 1(a), where the leptomeninges [Fig. 1(a), white arrow] can be clearly distinguished as a very thin layer above the gray matter. The rest of the tissue appears almost homogeneous on the tomogram with no distinctly visible layers or smaller morphological details. Comparison with corresponding H&E-stained histological sections [Figs. 1(b) and 1(c)] shows that the human isocortex has a layered structure with no distinctly outlined borders between the different layers. Both histological sections also reveal that the density of neuronal and glial somas with typical size of the nuclei [indicated with white arrows in Fig. 1(c)] ~5 $\mu$m or less, is very low in the first layer of the gray matter, and that it increases significantly in layer II. The thickness of layer I of the human isocortex varies with location and typically ranges between 100 and 500 $\mu$m, and in this particular case appears to be ~300 $\mu$m.

In addition to healthy brain tissue three different types of meningiomas and one type of ganglioglioma were imaged. Figure 2(a) shows a representative OCT tomogram acquired from a fibrous meningioma biopsy, while the corresponding H&E-stained histological section is presented in Fig. 2(b). Under the current imaging conditions ($\lambda_c \sim 800$ nm, $P_{sample} = 5$ mW, and SNR = 112 dB) the image penetration depth in the fibrous meningioma tissue appears limited to about 400 $\mu$m, and no structural details can be distinguished deeper in the sample. The dark horizontal line in the tomogram is an imaging artifact. At shallow depths up to ~250 $\mu$m, clusters of highly reflective (black) spots are distinctly visible even

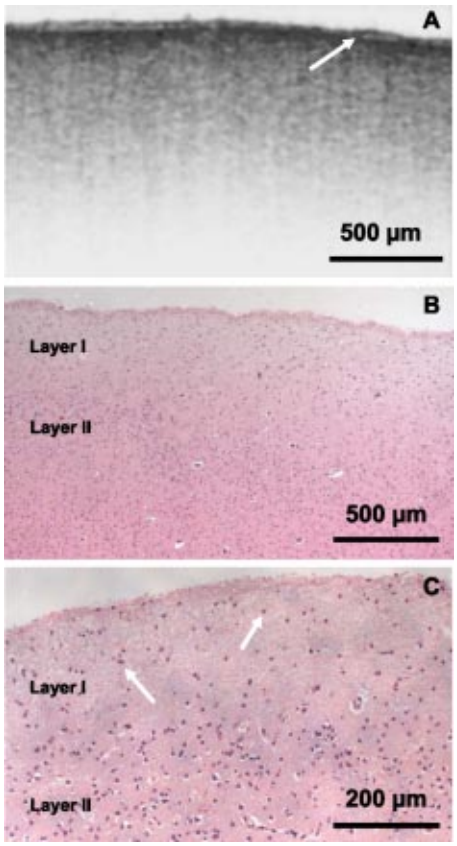


**Fig. 1** (a) UHR OCT tomogram (2×1.35 mm) of healthy brain tissue acquired with resolution of 0.9×2 $\mu$m (axial×lateral) at $\lambda_c = 800$ nm and (b) and (c) representative H&E-stained histological sections. The arrow in (a) indicates the leptomeningi, while the white arrows in (c) indicate the neuron and glial cell nuclei.

after application of a speckle reduction[36,37] image processing algorithm (oversampling of the acquired data—20-nm separation between adjacent points in a single A-scan, 0.5-$\mu$m separation between adjacent A-scans, and subsequent application of directional spatial averaging). An enlarged view [Fig. 2(c)]

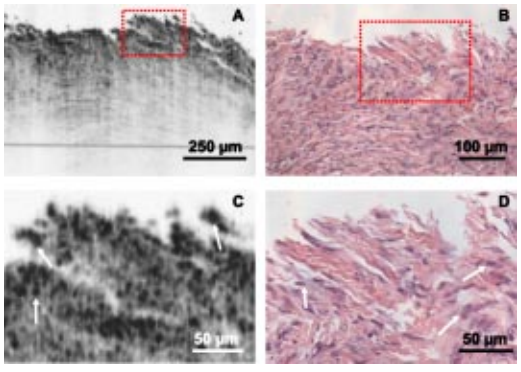


**Fig. 2** UHR OCT tomogram (1×0.69 mm) of (a) fibrous meningioma and (b) corresponding H&E-stained histological section, (c) an enlarged view of the region in the tomogram (a) marked with the red dotted line and (d) a proportional enlargement of the histological image. White arrows in (c) and (d) indicate enlarged nuclei of tumor cells.

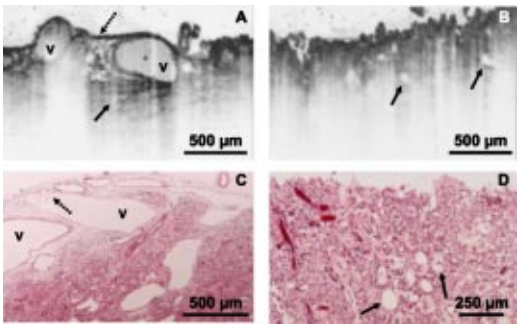


**Fig. 3** UHR OCT tomograms (2×1.25 mm) of atypical meningioma acquired from (a) the surface of the tumor and (b) a region within the tumor; (c) and (d) corresponding H&E-stained histological sections. Blood vessels are marked with the letter V; the leptomeningi, with dashed arrows; and the microcysts, with black arrows.

of a selected region in the biopsy sample, marked with red dotted line in Fig. 2(a) shows that the black spots (marked with white arrows) vary in shape and range in size between 5 and 15 $\mu$m. A magnified view of the histological section [Fig. 2(d)] reveals that the nuclei of tumor cells are about two to five times larger than the nuclei of normal neuron/glial cells, and that they fill up to ~80% of the cell volume. Since cell nuclei are optically much denser than the cell cytoplasm, they scatter light more strongly. Therefore it is very likely that the highly reflective black spots observed in the UHR OCT tomogram correspond to enlarged nuclei of tumor cells (marked with white arrows). The fact that no highly reflective small spots are visible on the OCT tomogram beyond a depth of ~300 $\mu$m most probably results from loss of contrast and resolution with imaging depth.

Figure 3 shows two representative UHR OCT tomograms of atypical meningioma acquired from the surface of the tumor [Fig. 3(a)] and from a region within the tumor [Fig. 3(b)], along with the corresponding H&E-stained histological sections [Figs. 3(c) and 3(d)]. The surface of the atypical meningioma is highly vascularized and Fig. 3(a) shows that UHR OCT is able to visualize both the meninges (marked with dashed black arrow) and a number of blood vessels (marked with letter V) ranging in diameter from ~50 to ~400 $\mu$m. In addition, shadows of microcysts positioned below the largest blood vessel (see black arrow) are also discernable in the OCT tomogram. Although the histological section presented in Fig. 3(c) is not an exact match for the location at which the optical image was acquired, it does show morphological features very similar to those observed in the OCT tomogram. Similarly, the image acquired from a region within the atypical meningioma [Fig. 3(b)] shows an abundance of cysts (marked with black arrows) ranging in size between 20 and 100 $\mu$m, which corresponds well to the tissue morphology as visualized in the histological section [Fig. 3(d)].

Figure 4 shows representative UHR OCT tomograms of a transitional meningioma acquired at two different locations in the biopsy sample [Figs. 4(a) and 4(b)]. In addition to presence of large cysts (marked with black arrows), both images show morphological features in the shape of spheres and spirals [marked with the red dotted lines in Figs. 4(a) and 4(b) and white arrows in Figs. 4(c) to 4(e)], composed of striplike clusters of highly reflective black spots [see Figs. 4(d) and

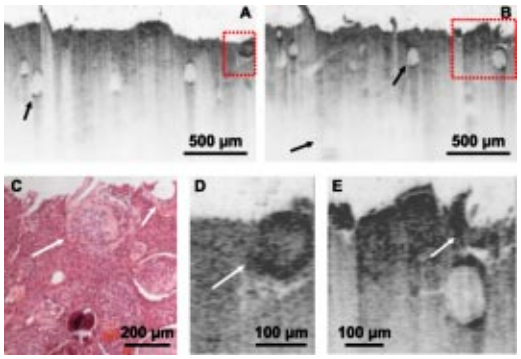


**Fig. 4** (a) and (b) UHR OCT tomograms (2×1.25 mm) of transitional meningioma acquired from different locations at the surface of the tumor; (c) representative H&E-stained histological section; (d) and (e) enlarged views of the regions marked with red dotted lines in (a) and (b), correspondingly. The black arrows indicate microcysts, and the white arrows, round and spiral-shaped clusters of collagen fiber matrix and imbedded groups of tumor cells.

4(e), which are magnified copies of the regions marked with the red dotted lines in Figs. 4(a) and 4(b)]. Comparison with H&E-stained histology [Fig. 4(c)] shows strips of collagen matrix alternating with groups of tumor cells bundled together in clusters of spherical or spiral shape (see white arrows). The clusters appear to vary in size between 50 and 500 $\mu$m in diameter, which is in good agreement with the morphological features observed in the OCT tomograms.

Figure 5(a) shows a representative UHR OCT tomograms of ganglioglioma in which regions containing clusters of highly reflective black spots are distinctly visible. A magnified copy of a selected region from the OCT image, marked with a red dotted line is presented in Fig. 5(b). It shows striplike groups of highly reflective spots (marked with white arrows) alternating with low-back-scattering regions (pale gray color). Comparison with stained H&E histology [Fig. 5(c)] shows that in this specimen tumor cells tend to group in striplike clusters (marked with white arrows) separated from each other by layers of collagen matrix.

## 4 Discussion

Morphologically, pathological brain tissue is characterized by abundance of tumor cells with enlarged nuclei, microcalcifications, cysts, and enhanced vascularization—features that are normally absent in healthy brain tissue. For OCT to be successfully applied as an *in vivo* optical biopsy tool in neurosurgery, capable of discriminating between healthy and pathological brain tissue, visualization of tumor cells or larger morphological features positioned at various depths within the tissue is required. This necessitates micrometer-scale OCT resolution maintained within millimeter-range penetration depth. In free space, the OCT lateral resolution $\Delta x$ is dependent both on the optical characteristics of the light source $(\lambda_c, \Delta\lambda)$ and the magnification properties of the imaging optics (focal length $f$ and beam diameter $D$), while the OCT axial resolution $\Delta z$ is determined solely by the spectral characteristics of the light source[16,18] $(\Delta z \sim \lambda_c^2/\Delta\lambda)$. In biological tissue, the OCT image resolution in both directions is affected by wavefront distortions in the focused optical beam resulting from wavelength-dependent scattering of light from cell

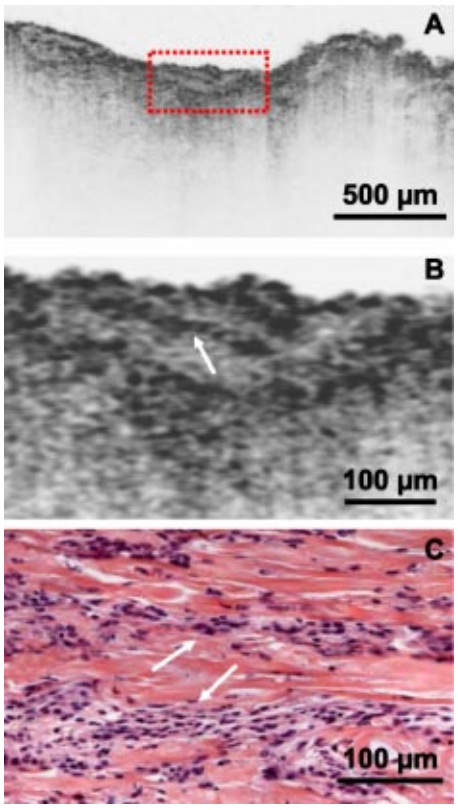


**Fig. 5** (a) UHR OCT tomogram (2×1 mm) of ganglioglioma, (b) an enlarged view of the region marked with red dotted line in (a), and (c), the corresponding H&E-stained histological section. The white arrows indicate strip-shaped clusters of tumor cells.

membranes and subcellular components. Scattering of light is also one of the major factors that determine the image penetration depth within biological tissue, which is scaled as $1/\lambda_c^k$, where the coefficient $k$ is dependent on the size, shape, and relative refractive index of the scattering particles.[38] The existing trade-off between OCT spatial resolution and image penetration depth as functions of wavelength is typically resolved depending on which imaging parameter priority is set on. Since this study aimed to investigate the ability of UHR OCT to visualize morphological features as small as 5 to 10 $\mu$m in diameter, priority was placed on providing micrometer-scale resolution that would enable imaging of single tumor cells. So far, submicrometer axial resolution OCT has been realized in the visible[15] and the 800-nm wavelength range[39] using a photonic crystal fiber (PCF)-based light source and a Ti:$Al_2O_3$ laser, respectively. However, the spectral stability and the OCT sensitivity were superior in the case of the Ti:$Al_2O_3$ laser, which determined the choice of light source in this study. Image penetration depths ranging from 400 $\mu$m in the fibrous meningioma sample [Fig. 2(a)] to about 1 mm in the transitional meningioma biopsy were achieved by using the state-of-the-art Ti:$Al_2O_3$ laser (SNR=112 dB for 5-mW incident power).

The micrometer-scale OCT spatial resolution achieved by employing the broad-bandwidth Ti:$Al_2O_3$ laser in this study enabled detailed visualization of small morphological features, i.e., clear delineation of the shape of small 20- to 50-$\mu$m cysts (see Figs. 3 and 4). In addition, the UHR OCT

images of fibrous meningioma and ganglioglioma shown in Figs. 2 and 5 displayed numerous highly reflective black spots, ranging in size between 5 and 20 $\mu$m at depths up to 100 to 150 $\mu$m in tissue. In the case of ganglioglioma [Fig. 5(b)] the reflective spots appear clustered in strips, alternating with low-backscattering background, which correlates closely with the morphology of this type of tumor tissue, as shown in the corresponding histological image [Fig. 5(c)]. To investigate the origin of the reflective spots, we performed an image speckle analysis. The use of partially incoherent light source with a 260-nm bandwidth reduces significantly the probability of detection of multiply scattered, wide-angle, out-of-focus light, especially at shallow imaging depths of 100 to 150 $\mu$m in brain tissue, and consequently suppresses generation of small ($\sim\lambda_c$ or less) size noiselike speckle pattern. The average speckle size in the raw UHR OCT images was of the order of tens of micrometers, which suggested that it most likely originated from small-angle scattered light within the focal volume. This type of speckle pattern in addition to containing a noise component is also related to the imaged tissue morphology.[36] The appearance of both wide-angle, noiselike and small-angle speckle patterns can be reduced by application of various speckle reduction techniques. On this particular occasion, we used data acquisition oversampling and subsequent directional spatial compounding to achieve better image quality. The appearance of the highly reflective spots in the UHR OCT tomograms of selected neuropathologies (Figs. 2 and 5) even after the application of the speckle reduction algorithm, and their absence in the OCT images of healthy brain tissue suggested that the reflective spots may be related to real morphological features characteristic of pathological brain tissue. A close comparison between the UHR OCT tomograms presented in Figs. 2(c) and 5(b) and the corresponding histological images [Figs. 2(d) and 5(c)] shows that both neuropathologies are characterized with abundance of tumor cells with enlarged nuclei. Extensive previous research[40] has demonstrated that the magnitude and angular distribution of light scattered from cells strongly depends on the size, shape, and chromatin texture of the cell nucleus. Normal cell nuclei typically have finely distributed chromatin texture, while typical features or tumor cell nuclei are of a larger size, usually have a distorted elongated shape, and include the presence of dense clusters of chromatin fibers. The magnitude of light scattered from abnormally large tumor cell nuclei is significantly enhanced at angles close to 0 and 180 deg as compared to the case of light scattered from normal cell nuclei. Since UHR OCT preferentially detects ballistic and small-angle single scattered light at imaging depths of few hundred micrometers in highly scattering brain tissue, it is very likely that the highly reflective black spots observed in Figs. 2(c) and 5(b) correspond to light scattered from tumor cell nuclei. This hypothesis, although very probable, should be tested in the future by imaging isolated cells with UHR OCT and comparing the images with stained histological cross sections.

The ability of UHR OCT to resolve small morphological features diminishes with depth in biological tissue and for the specific neuropathologies discussed in this paper appears to be limited to depths of $\sim$100 to 150 $\mu$m. Moreover, no neuron or glial cells were distinguished in the healthy human brain tomograms. The sparse distribution of neuron and glial somas in layer I of the normal human isocortex [see Fig. 1(c)] and the loss of image contrast with depth in the sample can only partially account for the fact that cell nuclei are not resolved in the healthy brain UHR OCT tomogram. The deterioration of OCT spatial resolution with depth in biological tissue is the most likely cause for the depth-dependent loss of UHR OCT resolving power. Since the axial OCT resolution is mainly determined by the coherence length of the light source, it is practically insensitive to spherical aberrations, arising from focusing the optical beam in tissue—a medium with spatially varying index of refraction. Moreover, although human healthy brain tissue is highly scattering at $\lambda_c \sim 800$ nm, at shallow imaging depths smaller than 200 $\mu$m, UHR OCT detects preferentially ballistic backscattered light, and thus, the axial resolution should not be affected significantly by detection of multiply scattered light. However, the lateral OCT resolution is determined by the imaging optics and therefore is more susceptible to spherical aberrations of the optical beam focused in the tissue, which should become more pronounced with the depth in the imaged sample. Possible ways to counteract the deteriorating effect of tissue optical properties on the OCT image resolution include developing of better dynamic focusing techniques as well as merging of UHR OCT with adaptive optics,[41] which may be able to partially correct the wavefront aberrations in the optical beam caused by the spatial variations in the tissue refractive index.

The results presented in this paper clearly demonstrate the ability of UHR OCT to distinguish between healthy and pathological human brain tissue by visualization of fine morphological details such as the enlarged nuclei of tumor cells, microcalcifications, cysts, and microvasculature. However, these morphological features are often present in any neuropathology and therefore provide insufficient information for diagnosing the specific type of a brain tumor. To reach the diagnostic capabilities of standard histopathological methods, UHR OCT should be able to visualize morphology of normal and tumor cells within biological tissue. Future development of laser technology and the merging of OCT with adaptive optics may enable realization of isotropic submicrometer resolution within biological tissue that would enable the imaging of single cells. Furthermore, the development of new contrast agents for OCT may enable specific labeling of intracellular components, and thus enable discrimination between different types of brain tumors. Also, the development of laser technology in the near future may lead to novel ultra-broadbandwidth light sources with emission spectra centered in the 1300-nm wavelength region that may be able to provide submicrometer-scale axial OCT resolution at greater imaging depths in brain tissue. Since various neuropathologies are characterized with specific morphological and physiological changes occurring on a cellular level and considering the fact that the optical properties of biological tissue (scattering, absorption, scattering anisotropy) are related both to tissue morphology and physiology, employing tissue optics analysis in addition to the high-esolution morphological imaging may prove very beneficial for further extending the diagnostic capabilities of UHR OCT in neuropathology.

The results from this preliminary study have demonstrated that UHR OCT has a good potential for becoming a useful diagnostic tool for neuropathology. However, bringing this imaging method into the surgical room may encounter many challenges. For example, most brain tumors are larger than 1

mm in diameter and are typically located at depths greater than the maximum OCT image penetration depth (1 to 2 mm in optically dense tissue). In that case, they can be accessed optically only through a biopsy needle. Previous research[42] has demonstrated that the utilization of miniature optical components enables the construction of OCT imaging probes that can easily fit in a standard 27-gage biopsy needle. So far, OCT biopsy needles have been constructed to accommodate relatively narrow bandwidth light sources with emission spectra centered both at $\lambda_c \sim 800$ and $\lambda_c \sim 1300$ nm, although the proper selection of optical components should lead to an optical biopsy needle design suitable for UHR OCT. As a noninvasive, real-time optical biopsy tool UHR OCT may be used for better delineation of the boundaries of large brain tumors as well as for localization of clusters of tumor cells in the vicinity. The existing trade-off between the size of the imaged volume and the OCT spatial resolution can be solved in this case by combining macroscopic examination of large tissue surface/volume (coarse image resolution) aiming to visualize the large tumor boundary, and subsequent microscopic (submicrometer-resolution OCT) examination of small volumes of suspicious tissue. Further challenges posed to UHR OCT involve handling of motion artifacts and the presence of blood during neurosurgery. The effect of tissue movement can be counteracted by using high-speed image acquisition (for example, by employing a Fourier domain OCT technique), while the excess blood can be flushed out of the imaging field of view by using saline.

## 5 Conclusion

In summary, the aim of this research project was to investigate the diagnostic potential of UHR OCT in the field of neuropathology. The preliminary results presented in this paper clearly demonstrated that UHR OCT can successfully differentiate between healthy and pathological brain tissue. However, further technological advancements are required to improve the diagnostics capabilities of this imaging method and to further develop it as a noncontact, real-time optical biopsy diagnostic tool in neurosurgery.

### *Acknowledgments*

This research has been financially supported by FEMTOLASERS GmbH, Christian Doppler Society and by the following grants: FWF P14218-PSY, FWF Y 159-PAT, and CRAF-1999-70549.

### *References*

1. Hoffman, ''New advances in brain tumor imaging,'' *Curr. Opin. Oncol.* **13**, 148–153 (2001).
2. R. Acharya, R. Wasserman, J. Stevens, and C. Hinojosa, ''Biomedical imaging modalities: a tutorial,'' *Comput. Med. Imaging Graph.* **19**, 3–25 (1995).
3. P. M. Black, T. Moriatry, E. Alexander, P. Stieg, E. J. Woodard, P. L. Gleason, C. H. Martin, R. Kikinis, R. B. Schwartz, and F. A. Jolesz, ''Development and implementation of intraoperative magnetic resonance imaging and its neurological applications,'' *Neurosurgery* **41**, 831–845 (1997).
4. N. A. Sharif and M. E. Lewis, Eds. *Brain Imaging*, Ellis Horwood Ltd. (1989).
5. W. F. Chandler, J. E. Knake, J. E. McGillicuddy, K. O. Lillehei, and T. M. Silver, ''Intra-operative use of real-time ultrasonmography in neurosurgery,'' *J. Neurosurg.* **57**, 157–163 (1982).
6. D. R. Enzmann, R. Wheat, W. H. Marshall, R. Bird, K. Murphy-Irwin, K. Karbon, J. Hanbery, C. D. Silverberg, R. H. Britt, and L. Shuer, ''Tumors of the central nervous system studied by computed tomography and ultrasound,'' *Radiology* **154**, 393–399 (1985).
7. M. J. Taphoorn, J. J. Heimans, M. C. Kaiser, R. G. de Slegte, F. C. Crezee, and J. Valk, ''Imaging of brain metastases:comparison of computerized tomography (CT) and magnetic resonance imaging (MRI),'' *Neuroradiology* **31**, 391–395 (1989).
8. G. A. W. Gooding, J. E. Boggan, and P. R. Weinstein, ''Characterization of intracranial neoplasms by CT and intraoperative sonography,'' *AJNR Am. J. Neuroradiol.* **5**, 517–520 (1984).
9. M. Scholz, M. Deli, U. Windforster, K. Wentz, A. Recknagel, H. Preuschoft, and A. Harders, ''MRI-guided endoscopy in the brain: a feasibility study,'' *Minim Invasive Neurosurg.* **2**, 33–37 (1996).
10. W. E. L. Grimson, G. J. Ettinger, S. J. White, T. Lozano.Perez, W. M. Wells, and R. Kikinis, ''An automatic registration method for freameless steretaxy, image-guided surgery and enhanced reality visualization,'' *IEEE Trans. Med. Imaging* **15**, 129 (1996).
11. A. Mizuno, T. Hayashi, K. Tashibu, S. Maruaishi, K. Kawauchi, and Y. Ozaki, ''Near-infrared Raman spectra of the rat brain tissues,'' *Neurosci. Lett.* **141**, 47–52 (1992).
12. D. A. Hansen, A. M. Spence, T. Carksi, and M. S. Berger, ''Indocyanine green (ICG) staining and demarcation of tumor margins in a rat glioma model,'' *Surg. Neurol.* **40**, 451–456 (1993).
13. W. S. Poon, K.-T. Schomacker, T. F. Deutsch, and R. L. Martuza, ''Laser induced fluorescence: experimental intraoperative delineation of tumor resection margins,'' *J. Neurosurg.* **76**, 679–686 (1992).
14. M. M. Haglund, D. W. Hochman, A. M. Spence, and M. S. Berger, ''Enhanced optical imaging of rat gliomas and tumor margins,'' *Neurosurgery* **35**, 930–941 (1994).
15. P. Jeannesson, M. Manfait, and J. C. Jardillier, ''A technique for laser Raman spectroscopic studies of isolated cell populations.''
16. D. Huang, E. A. Swanson, C. P. Lin, J. S. Schuman, W. G. Stinson, W. Chang, M. R. Hee, T. Flotte, K. Gregory, C. A. Puliafito, and J. G. Fujimoto, ''Optical coherence tomography,'' *Science* **254**, 1178–1181 (1991).
17. J. G. Fujimoto, M. Brezinski, G. Tearney, S. A. Boppart, B. Bouma, M. Hee, J. Southern, and E. Swanson, *Nat. Med.* **1**, 970–972 (1995).
18. A. F. Fercher, ''Optical coherence tomography,'' *Biomed. Opt.* **1**, 157–173 (1996).
19. B. Bouma and J. Tearney, Eds., *Handbook of Optical Coherence Tomography*, Marcel Dekker (2002).
20. S. A. Boppart, M. Brezinski, C. Pitris, and J. G. Fujimoto, ''Optical coherence tomography for neurosurgical imaging of human intracortical melanoma,'' *Neurosurgery* **43**, 834–841 (1998).
21. R. Uma Maheswari, H. Takaoka, R. Homma, H. Kadono, and M. Tanifuji, ''Implementation of optical coherence tomograohy (OCT) in visualization of functional structures of cat visual cortex,'' *Opt. Comm.* **202**, 47–54 (2002).
22. M. Lazebnik, D. L. Marks, K. Potgieter, R. Gillette, and S. A. Boppart, ''Functional optical coherence tomography for detecting neural activity through scattering changes,'' *Opt. Lett.* **28**, 1218–1220 (2003).
23. S. Roper, M. D. Morgner, G. V. Gelikonov, F. I. Feldchtein, N. M. Beach, M. A. King, V. M. Gelikonov, A. M. Sergeev, and D. H. Reitze, ''*In-vivo* detection of experimentally induced cortical dygenesys abnormality in the adult rat neocortex using optical coherence tomography,'' *J. Neurosc. Meth.* **80**, 91–98 (1998).
24. W. Drexler, U. Morgner, F. X. Kärtner, C. Pitris, S. A. Boppart, X. D. Li, E. P. Ippen, and J. G. Fujimoto, ''*In-vivo* ultrahigh resolution optical coherence tomography,'' *Opt. Lett.* **24**, 1221–1223 (1999).
25. I. Hartl, X. D. Li, C. Chudoba, R. K. Ghanta, T. H. Ko, J. G. Fujimoto, J. K. Ranka, and R. S. Windeler, ''Ultrahigh resolution optical coherence tomography using continuum generation in an air-silica microsctructure optical fiber,'' *Opt. Lett.* **26**, 608–610 (2001).
26. B. Považay, K. Bizheva, A. Unterhuber, B. Herman, H. Sattmann, A. Fercher, W. Drexler, A. Apolonski, W. J. Wadsworth, J. C. Knight, P. S. J. Russel, M. Vetterlein, and E. Scherzer, ''Sub-micrometer resolution optical coherence tomography,'' *Opt. Lett.* **27**, 1800–18024 (2002).
27. L. Vabre, A. Dubois, and A. C. Boccara, ''Thermal light full-field optical coherence tomography,'' *Opt. Lett.* **27**, 530–532 (2002).
28. K. Bizheva, B. Povazay, B. Hermann, H. Sattmann, W. Drexler, M. Mei, R. Holzwarth, T. Hoelzenbein, V. Wacheck, and H. Pehamberger, ''Compact, broad bandwidth fiber laser for sub-2 $\mu$m axial resolution optical coherence tomography in the 1300 nm wavelength region,'' *Opt. Lett.* **28**, 707–709 (2003).

29. A. Unterhuber, B. Povazay, B. Hermann, H. Sattmann, V. Yakovlev, G. Tempea, C. Schubert, E. M. Anger, P. K. Ahnelt, M. Stur, J. E. Morgan, A. Cowey, G. Jung, T. Le, A. Stingl, and W. Drexler, ''Compact low-cost Ti:$Al_2O_3$ laser for *in-vivo* ultrahigh-resolution optical coherence tomography,'' *Opt. Lett.* **28**, 905–907 (2003).
30. W. Drexler, ''Ultrahigh resolution optical coherence tomography,'' *J. Biomed. Opt.* **9**, 47–74 (2004).
31. W. Drexler, U. Morgner, R. K. Ghanta, J. S. Schuman, F. Kärtner, and J. G. Fujimoto, ''Ultrahigh-resolution ophthalmic optical coherence tomography,'' *Nature Med.* **7**, 502–507 (2001).
32. M. Gloesmann, B. Hermann, C. Schubert, H. Sattmann, P. K. Ahnelt, and W. Drexler, ''Histologic correlation of pig retina radial stratification with ultrahigh-resolution optical coherence tomography,'' *Invest. Opthalmol. Visual Sci.* **44**, 1696–1703 (2003).
33. W. Drexler, H. Sattmann, B. Hermann, T. K. Ko, M. Stur, A. Unterhuber, C. Scholda, O. Findl, M. Wirtitsch, J. G. Fujimoto, and A. F. Fercher, ''Enhanced visualization of macular pathology with the use of ultrahigh-resolution optical coherence tomography,'' *Arch. Ophthalmol. (Chicago)* **121**, 695–706 (2003).
34. K. Bizheva, A. Unterhuber, B. Hermann, B. Povazay, H. Sattmann, W. Drexler, A. Stingl, T. Le, M. Mai, R. Holzwarth, H. A. Reitsamer, J. E. Morgan, and A. Cowey, ''Imaging *ex-vivo* and *in-vitro* brain morphology in animal models with ultrahigh resolution optical coherence tomography,'' *J. Biomed. Opt.* **9**, 719–724 (2004).
35. T. Fuji, A. Unterhuber, V. S. Yakovlev, G. Tempea, F. Krausz, and W. Drexler, ''Generation of smooth, ultra-broadband spectra directly from a prism-less Ti:sapphire laser,'' *Appl. Phys. (Berlin)* , (2003).
36. J. M. Schmitt, S. H. Xiang, and K. M. Yung, ''Speckle in optical coherence tomography,'' *J. Biomed. Opt.* **4**, 95–105 (1999).
37. F. A. Sadjadi, ''Perspective on techniques for enhancing speckle imagery,'' *Opt. Eng.* **29**, 25–30 (1990).
38. J. M. Schmitt and G. Kumar, ''Optical scattering properties of soft tissues: a discrete particle model,'' *Appl. Opt.* **37**, 2788–2797 (1998).
39. A. Unterhuber, B. Povazay, K. Bizheva, B. Hermann, H. Sattmann, A. Stingl, T. Le, M. Seefeld, R. Menzel, M. Preusser, H. Budka, C. Schubert, H. Reitsamer, P. K. Ahnelt, J. E. Morgan, A. Cowey, and W. Drexler, ''Advances in broad bandwidth light sources for ultrahigh resolution optical coherence tomography,'' *Phys. Med. Biol.* **49**, 1235–1246 (2004).
40. R. Drezek, M. Guillaud, T. Collier, I. Boiko, A. Malpica, C. Macaulay, M. Fallen, and R. Richards-Kortum, ''Light scattering from cervical cells through neoplastic progression: influence of nuclear morphology, DNA content, and chromatin texture,'' *J. Biomed. Opt.* **8**, 7–16 (2003).
41. A. Roorda, F. Romero-Borja, W. J. Donnelly III, H. Qeener, T. J. Herbert, and M. C. W. Campbell, ''Adaptive optics scanning laser ophthalmoscopy,'' *Opt. Express* **10**, 405–412 (2002).
42. X. Li, C. Chudoba, T. H. Ko, C. Pitris, and J. G. Fujimoto, ''Imaging needle for optical coherence tomography,'' *Opt. Lett.* **25**, 1520–1522 (2000).